Reynolds number effects and outer similarity of pressure fluctuations in turbulent pipe flow

Ming Yu[a,b], Alessandro Ceci[b], Sergio Pirozzoli[b]

[a]*State Key Laboratory of Aerodynamics, Mianyang 621000, China*
[b]*Dipartimento di Ingegneria Meccanica e Aerospaziale, Sapienza Universita di Roma, via Eudossiana 18, 00184 Roma, Italia*

Abstract

We study the structure of pressure fluctuations in turbulent pipe flow, up to friction Reynolds number $Re_\tau = 6000$, using standard spectral decomposition and proper orthogonal decomposition (POD). The mean pressure distribution is found to be qualitatively different from the case of channel flow, with an additional mean pressure difference caused by combined centrifugal and swirling effects. The variance of the pressure fluctuations exhibits a wide region with negative logarithmic decay with the wall distance, due to the presence of a hierarchy of wall-attached eddies, which we clearly trace in spectral maps, and which are generally isotropic in nature. On the other hand, the largest eddies are strongly non-isotropic, and are mainly elongated in the azimuthal direction. POD is used to prove self-similarity of the attached eddies, whose typical scales are found to be linearly proportional to the wall distance of their center.

Keywords: Pipe flow, pressure fluctuations, attached eddies

1. Introduction

Pressure fluctuations in wall-bounded turbulence have been widely investigated due to their important role in structural vibration and acoustic radiation [1]. Over the years, primary focus has been on assessing the variation of moments and spectral properties of pressure fluctuations against the Reynolds number in turbulent channels and boundary layers, whereas less is known about the case of pipe flow.

URL: yum16@tsinghua.org.cn (Ming Yu)

Early research on pressure fluctuations was commonly conducted via experimental methods. Readers may refer to Farabee and Casarella [2], Tsuji et al. [3], Klewicki et al. [4] for detailed and comprehensive literature review. However, it has been sometimes criticised that pressure fluctuation measurements in laboratory setups as wind tunnels and return circuits should be taken with caution owing to non-negligible spurious facility noise [5, 6]. The advent of direct numerical simulation (DNS) has provided an alternative and more accurate tool of investigations. However, experiments can achieve much higher Reynolds numbers, whereas DNS is still constrained by limitation of computational resources. This Reynolds number gap between experiments and simulations is being progressively filled on account of progress in computer science and algorithmic development.

It is by now well established that the intensity of wall pressure fluctuations in boundary layers and channels increases logarithmically with the Reynolds number, when scaled by the mean wall shear stress, say τ_w [7, 2, 8, 3, 9, 10]. Tsuji et al. [3] found a similar trend for the peak pressure variance, which occurs at approximated at $y^+ = 30$ (herein, the superscript + denotes the normalization by mean wall shear stress τ_w and kinematic viscosity ν). Jimenez and Hoyas [9] suggested that this logarithmic increment should be attributed to a growing hierarchy of self-similar wall-attached eddies [11, 12, 13]. Pressure, like the wall-parallel velocity components, can indeed be regarded as a wall-attached quantity [14], which explains why profiles of the pressure variance also follow a logarithmic trend with respect to the wall distance. The same behavior can however be also predicted based on inner/outer layer overlap arguments [15]. Mehrez et al. [16] explored the DNS database of turbulent channel flow at friction Reynolds number Re_τ ($= hu_\tau/\nu$, with h the channel height, $u_\tau = (\tau_w/\rho)^{1/2}$ the friction velocity, and ρ the fluid density) up to 4000, and found that the logarithmic trend only shows up for $Re_\tau \gtrsim 500$. Those authors showed that higher-order moments also follow the logarithmic behaviour. With the aid of conditional averaging, they found that pressure fluctuations are related to geometrically self-similar hairpin vortices, similar to those observed in experiments [17], and found through resolvent analysis [18]. Sillero et al. [10], Panton et al. [15] compared the pressure fluctuation intensity profiles in turbulent channels, pipes and zero-pressure-gradient boundary layers, and found that the disparity primarily lies in the outer region, where the effects of the flow geometry cannot be disregarded.

By inspecting the spatial spectra, Jimenez and Hoyas [9] pointed out that there are two sorts of flow structures related to pressure fluctuations, the strongest being localized in the near-wall region, and weaker large-scale structures spanning the entire wall layer. The former scale in viscous coordinates, whereas the latter scale in outer coordinates. Tsuji et al. [19] argued about the possible onset of a secondary peak of the pressure variance in the outer wall region, as for the streamwise velocity variance. However, such peak is not observed in channel flow [16]. Within the overlap region, the characteristic length scales of pressure fluctuations in the streamwise and spanwise directions increase linearly with the wall-normal location [16], reminiscent of the self-similar features of the attached eddies. A recent study by Xu et al. [20] combined the Kolmogorov theory and the attached eddy hypothesis formalism to show that the pre-multiplied pressure spectra in the logarithmic layer should follow distinct power laws at small and at large scales, which at sufficiently high Reynolds number would reduce to k^{-1} variation at the large scales, and $k^{-7/3}$ variation at the small scales, where k is a relevant wavenumber.

The consensus reached so far is mostly based on turbulent channel flows and boundary layers. Although pipes are supposed to behave similarly to channels, some differences are nevertheless noted [10], which should be most apparent in the outer wall layer. In the present study we thus focus on the study of pressure fluctuations in turbulent pipe flow. By exploiting the database introduced in a previous study [21], herein we investigate the variation of intensities and spectral properties of pressure fluctuations in a relatively wide range of Reynolds number. Utilizing a standard tool of analysis as proper orthogonal decomposition (POD), we further investigate off-wall similarity of pressure-bearing eddies. The remainder of this paper is organized as follows. In Section 2 we present the numerical database; the one-point statistics and the spatial organization of the pressure field are discussed in Section 3 and 4, respectively. Energetic modes extracted from POD are presented in Section 5. Concluding comments are finally given in Section 6.

2. The DNS database

Numerical simulations of fully developed turbulent flows in a circular pipe are carried out assuming periodic boundary conditions in the axial (z) and azimuthal (ϕ) directions, as shown in figure 1. The velocity field is controlled by two parameters, namely the bulk Reynolds number ($Re_b = 2Ru_b/\nu$, with R the pipe radius

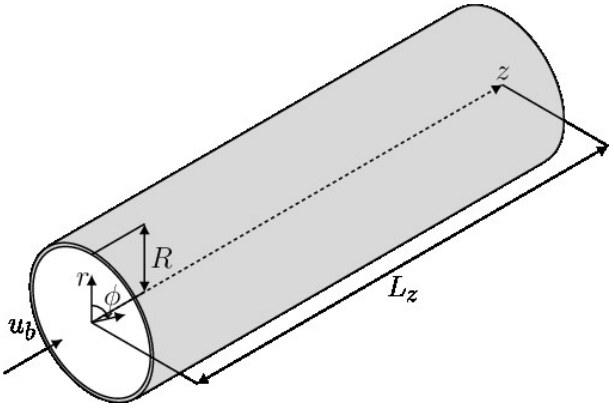

Figure 1: Definition of coordinate system for DNS of pipe flow. z, r, ϕ are the axial, radial and azimuthal directions, respectively. R is the pipe radius, L_z the pipe length, and u_b is the bulk velocity.

and u_b the bulk velocity), and the relative pipe length, L_z/R. The incompressible Navier-Stokes equations are solved with a spatially uniform, time-varying pressure gradient in such a way that the mass flow rate is kept strictly constant in time. A second-order finite-difference discretization of the incompressible Navier-Stokes equations in cylindrical coordinates is used, based on the classical marker-and-cell method [22], whereby pressure and passive scalars are located at the cell centers, whereas the velocity components are located at the cell faces, thus removing odd-even decoupling phenomena and guaranteeing discrete conservation of the total kinetic energy in the inviscid limit. The Poisson equation resulting from enforcement of the divergence-free condition is efficiently solved by double trigonometric expansion in the periodic axial and azimuthal directions, and inversion of tridiagonal matrices in the radial direction [23]. A crucial issue is the proper treatment of the polar singularity at the pipe axis. A detailed description of the subject is reported in Verzicco and Orlandi [24], but basically, the radial velocity u_r in the governing equations is replaced by $q_r = ru_r$ (r is the radial space coordinate), which by construction vanishes at the axis. The governing equations are advanced in time by means of a hybrid third-order low-storage Runge-Kutta algorithm, whereby the diffusive terms are handled implicitly, and convective terms in the axial and radial direction explicitly. An important issue in this respect is the convective time step limitation in the azimuthal direction, due to intrinsic shrinking of the cells size towards the pipe axis. To alleviate this limitation, we

Dataset	L_z/R	Mesh ($N_z \times N_r \times N_\phi$)	Re_b	Re_τ	$\Delta t_{stat}/\tau_t$	Line color
DNS-A	15	$256 \times 67 \times 256$	5300	180.3	204.0	
DNS-B	15	$768 \times 140 \times 768$	17000	495.3	87.4	
DNS-C	15	$1792 \times 270 \times 1792$	44000	1136.6	25.9	
DNS-D	15	$3072 \times 399 \times 3072$	82500	1976.0	22.4	
DNS-E	15	$4608 \times 540 \times 4608$	133000	3028.1	16.6	
DNS-F	15	$9216 \times 910 \times 9216$	285000	6019.4	8.32	

Table 1: Flow parameters for DNS of pipe flow. Cases are labeled in increasing order of Reynolds number, from A to F.

use implicit treatment of the convective terms in the azimuthal direction [25, 26], which enables marching in time with similar time step as in planar domains flow in practical computations. In order to minimize numerical errors associated with implicit time stepping, explicit and implicit discretizations of the azimuthal convective terms are linearly blended with the radial coordinate, in such a way that near the pipe wall the treatment is fully explicit, and near the pipe axis it is fully implicit. The code was adapted to run on clusters of graphic accelerators (GPUs), using a combination of CUDA Fortran and OpenACC directives, and relying on the CUFFT libraries for efficient execution of FFTs [27].

From now on, capital letters will used to denote flow properties averaged in the homogeneous spatial directions and in time, brackets to denote the averaging operator, and lower-case letters to denote fluctuations from the mean.

A list of the main simulations that we have carried out is given in table 1. The mesh resolution is designed based on the criteria discussed by Pirozzoli and Orlandi [28]. In particular, the collocation points are distributed in the wall-normal direction so that approximately thirty points are placed within $y^+ \leq 40$ ($y = R - r$ is the wall distance), with the first grid point at $y^+ < 0.1$, and the mesh is progressively stretched in the outer wall layer in such a way that the mesh spacing is proportional to the local Kolmogorov length scale, which there varies as $\eta^+ \approx 0.8\, y^{+1/4}$ [29]. Regarding the axial and azimuthal directions, finite-difference simulations of wall-bounded flows yield grid-independent results as long as $\Delta x^+ \approx 10$, $R^+\Delta\phi \approx 4.5$ [30], hence we have selected the number of grid points along the homogeneous flow directions as $N_z = L_z/R \times Re_\tau/9.8$, $N_\phi \sim 2\pi \times Re_\tau/4.1$. According to the established practice [31, 32, 33], the time

intervals used to collect the flow statistics (Δt_{stat}) are reported as a fraction of the eddy-turnover time (R/u_τ).

A detailed study of the velocity and passive scalar statistics are reported in previous studies [21, 34], which contain a full analysis of sensitivity of the flow statistics to domain size and grid resolution, as well as a study of the time sampling error. Based on the method of Russo and Luchini [35], which extends the classical batch means approach, we find that the sampling error for the one-point pressure statistics is generally quite limited, being larger in the largest DNS, which have been run for shorter time. In particular, in DNS-F the expected sampling error in the mean pressure and pressure variance is less than about 0.5%.

3. One-point pressure statistics

The mean pressure distribution in the radial direction is shown in figure 2(a,b), in terms of the difference between wall and local values. For all cases here considered the pressure difference first increases in the inner region, reaching a peak value, and then it decreases in the outer region. With the increase of the friction Reynolds number, the peak pressure difference increases, and the corresponding wall-normal location is shifted further away from the wall. For DNS-F, this peak resides at $y^+ \approx 1000$, or $y/R = 0.17$. This is rather different from the mean pressure in turbulent channel flows, as displayed in figure 2, in which the maxima of the mean pressure are reached in the inner region at $y^+ \approx 50 \sim 100$. The difference can be attributed to disparity in the respective mean balance equations. In turbulent channel flows, integration of the mean momemtum equation in the wall-normal direction yields

$$P_w - P(y) = \langle v^2 \rangle (y), \tag{1}$$

hence the distribution of the pressure difference is identical to the wall-normal velocity variance. In pipe flows, momentum balance along the radial direction yields [36]

$$\frac{\langle u_r^2 \rangle - \langle u_\theta^2 \rangle}{r} + \frac{\mathrm{d}\langle u_r^2 \rangle}{\mathrm{d}r} = -\frac{\mathrm{d}P}{\mathrm{d}r}, \tag{2}$$

which can be integrated to yield

$$P_w - P(y) = \underbrace{\langle u_r^2 \rangle}_{M_{r1}} + \underbrace{\int_0^y \frac{\langle u_r^2 \rangle - \langle u_\theta^2 \rangle}{R - y} \mathrm{d}y}_{M_{r2}}. \tag{3}$$

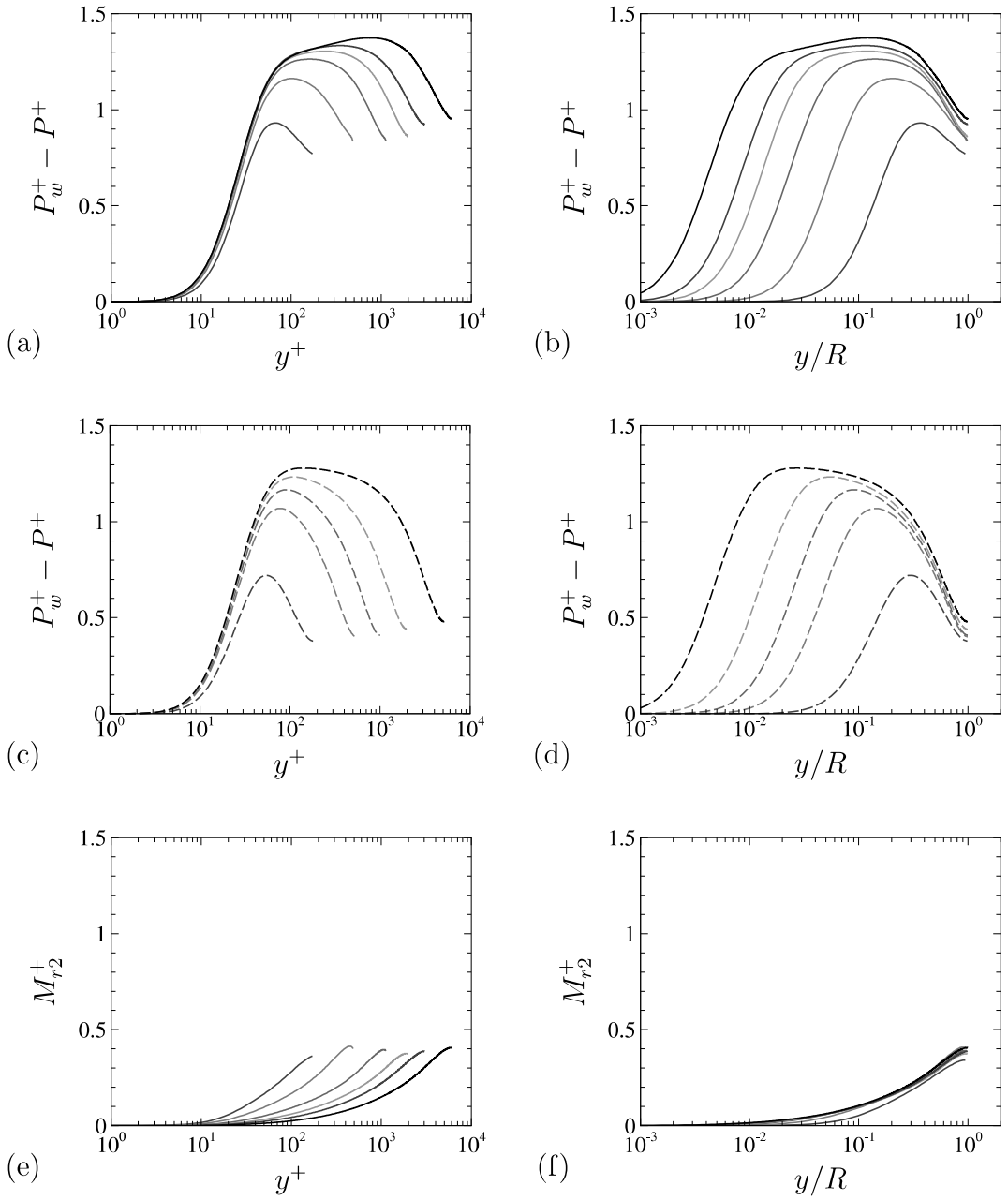

Figure 2: Wall-normal distribution of mean pressure difference in pipes (a-b) and in channels [32] at $Re_\tau = 180, 550, 1000, 2000, 5200$ (c-d, dashed lines), plotted against (a,c) viscous coordinates, and (b,d) outer coordinates. The M_{r2}^+ term in equation (3) is shown in panels (e-f). Refer to figure 1 for line style.

The first term is known to attain a flat distribution at high Reynolds number, and its peak value slowly asymptotes to an extrapolated values of about 1.38 in pipe flow [37]. The difference with respect to the case of channel flow is due to term M_{r2} at the right-hand-side of equation (3). The latter (see panels e,f) is associated with centrifugal $\langle u_r^2 \rangle$ and swirling $\langle u_\theta^2 \rangle$ effects, and is found to increase monotonically from the wall to the pipe centreline, hence it contributes to making the pressure difference between the pipe wall and the interior larger than in channel flow. Interestingly, term M_{r2} is scaling with very good approximation in outer units, yielding a maximum increase of about 0.4 wall units. As a consequence, we find that the difference between wall and centreline pressure to be of the order of one wall unit in the case of pipe flow, whereas in channels it is about 0.5 wall units.

The distributions of the pressure variance are displayed in figure 3(a-b). These are found to remain nearly constant within the viscous sublayer (say, $y^+ \leq 10$), then increasing to attain a peak value at $y^+ \approx 30$, and then decrease. A region with distinctly logarithmic decrease is found from $y^+ \approx 100$ to $y/R \approx 0.4$, which is then followed by steeper decrease towards the pipe centreline. As the Reynolds number increases, the pressure variances at the wall and their peak values increase systematically, whereas the centreline value is not much affected. When plotted against outer wall coordinates, the logarithmic portions of the pressure variance distribution collapse for $Re_\tau \gtrsim 500$, consistent with the case of channel flow [16]. Expressing the outer distribution as

$$\langle p^2 \rangle^+ (y/R) = A \log (y/R) + B, \tag{4}$$

curve fitting within the range of $y = (0.02 \sim 0.3)R$ for DNS-F yields the values of parameters $A = -2.28$ and $B = 1.13$, with error of 0.4%. Compared with the variances in turbulent channels (see figure 3(c)), we note that pressure fluctuations in pipes tend to be lower for $y^+ \lesssim 150$, and higher farther from the wall, a behavior which can also be traced in earlier studies [see, e.g. 10, figure 5]. Overall, the slope of logarithmic decay seems to be shallower in pipes. The calibrated log-law parameters are listed in table 2, along with those reported in previous studies in turbulent channels and boundary layers. Despite some data scatter across different studies, the table confirms that the decay rate is a bit less in pipes than in other flow configurations.

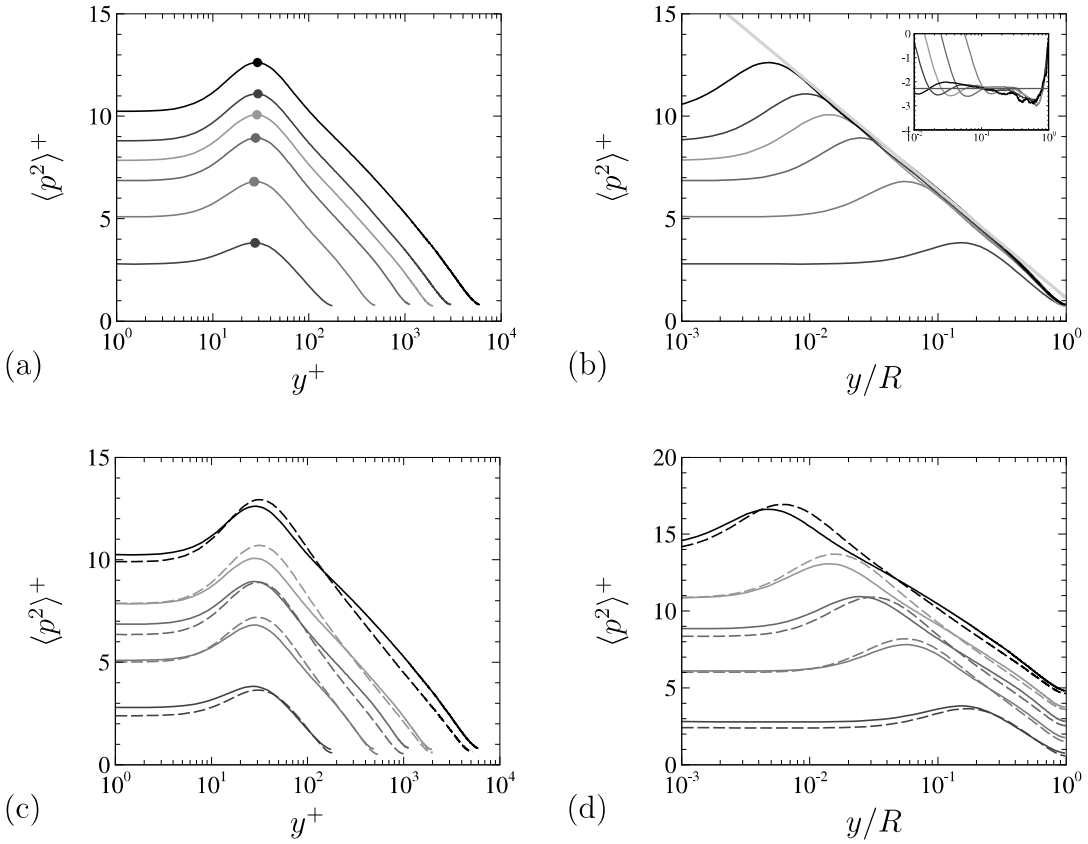

Figure 3: Wall-normal distribution of pressure variance plotted against (a) inner and (b) outer coordinates. Peaks values ($\langle p_P^2\rangle^+$) are marked with circles. In panel (b) the grey line denotes $\langle p^2\rangle^+(y/R) = A\log(y/R) + B$, with $A = -2.28$ and $B = 1.13$, and the inset shows the log-law diagnostic function, $y\,\mathrm{d}\left\langle p^2\right\rangle^+/\mathrm{d}y$. Panels (c,d) show a comparison with channel flow DNS data by Lee and Moser [32, dashed lines] at $Re_\tau = 180, 550, 1000, 2000, 5200$, offset by 2.0 in (d). Refer to figure 1 for line style.

Table 2: Parameters of logarithmic fits for pressure variance distributions in equation (4).

Source	A	B
Pipe (present)	-2.28	1.13
Channel [10]	-2.75	0.1
Channel [15]	-2.56	0.270
Channel [16]	-2.51	0.395
Boundary layer [16]	-2.42	2.39

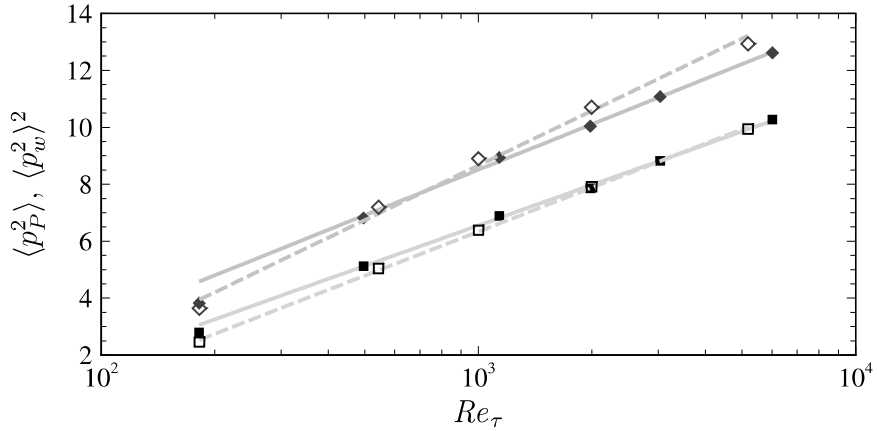

Figure 4: Variation of wall pressure variance ($\langle p_w^2 \rangle^2$, black squares) and peak pressure variance ($\langle p_P^2 \rangle$, red diamonds) with Re_τ. Solid symbols are used for pipe flow (present DNS), and open symbols for channel flow [32]. Solid lines note the fits given in equation (5) and (6). The dashed lines denote data fits for channel flow [16], $\langle p_w^2 \rangle^+ = 2.24 \log(Re_\tau) - 9.18$, $\langle p_P^2 \rangle^+ = 2.77 \log(Re_\tau) - 10.47$.

We further report the wall and peak values of pressure variances $\langle p_w^2 \rangle^+$ and $\langle p_P^2 \rangle^+$ in figure 4. With exclusion of the lowest Reynolds number case at $Re_\tau \approx 180$, the wall and peak values of pressure variances can be well characterized in terms of the following logarithmic trends

$$\langle p_w^2 \rangle^+ = 2.05 \log(Re_\tau) - 7.61, \tag{5}$$

$$\langle p_P^2 \rangle^+ = 2.22 \log(Re_\tau) - 6.74. \tag{6}$$

The data thus support theoretical inference that wall and peak pressure variances increase logarithmically with Re_τ, with accuracy of 0.3% and 0.25%, respectively. The logarithmic growth rate seems to be marginally, but systematically less than for channel flow, which again highlights differences between the two flows.

4. Spatial organization

Representative instantaneous fluctuating pressure fields are shown in figure 5, at the pipe wall and in the cross section. At low Reynolds number pressure fluctuations are organized into nearly circular blobs, but some hint of coherence along the azimuthal is also perceivable. This kind of organization is distinctly different than in the axial velocity field, which is instead characterized by longitudinal

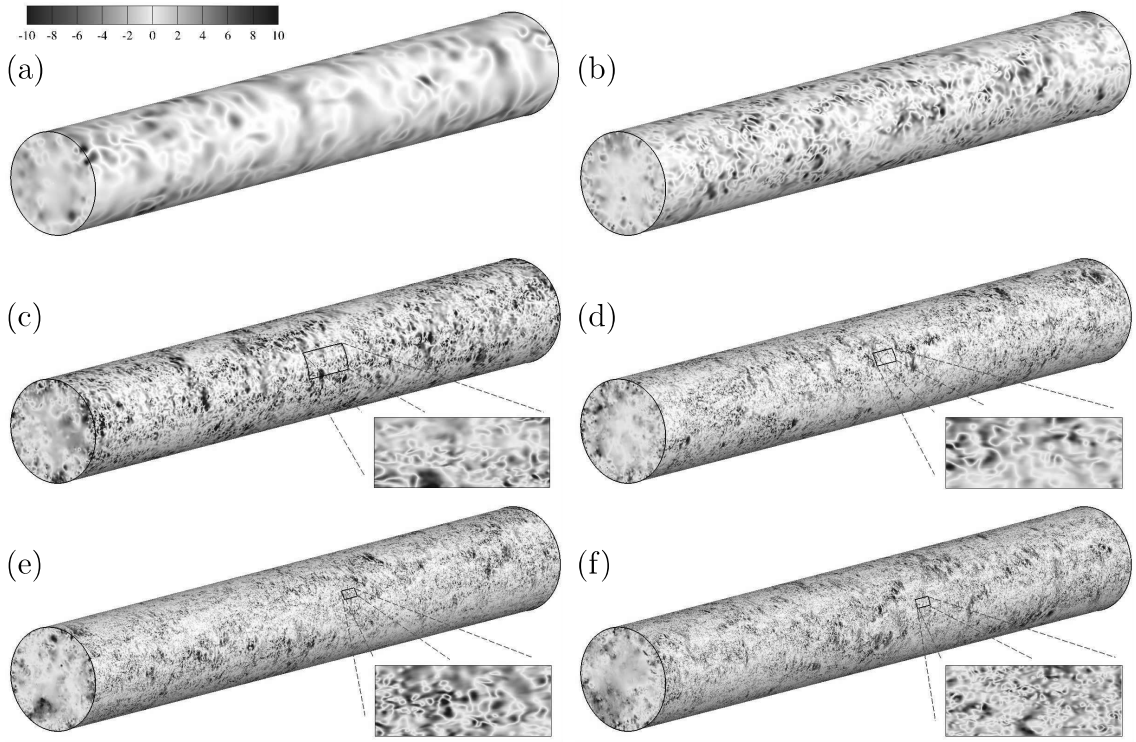

Figure 5: Instantaneous fields of inner-scaled pressure fluctuations (p/τ_w) at the pipe boundary and in the cross section, for (a) DNS-A, (b) DNS-B, (c) DNS-C, (d) DNS-D, (e) DNS-E, (f) DNS-F.

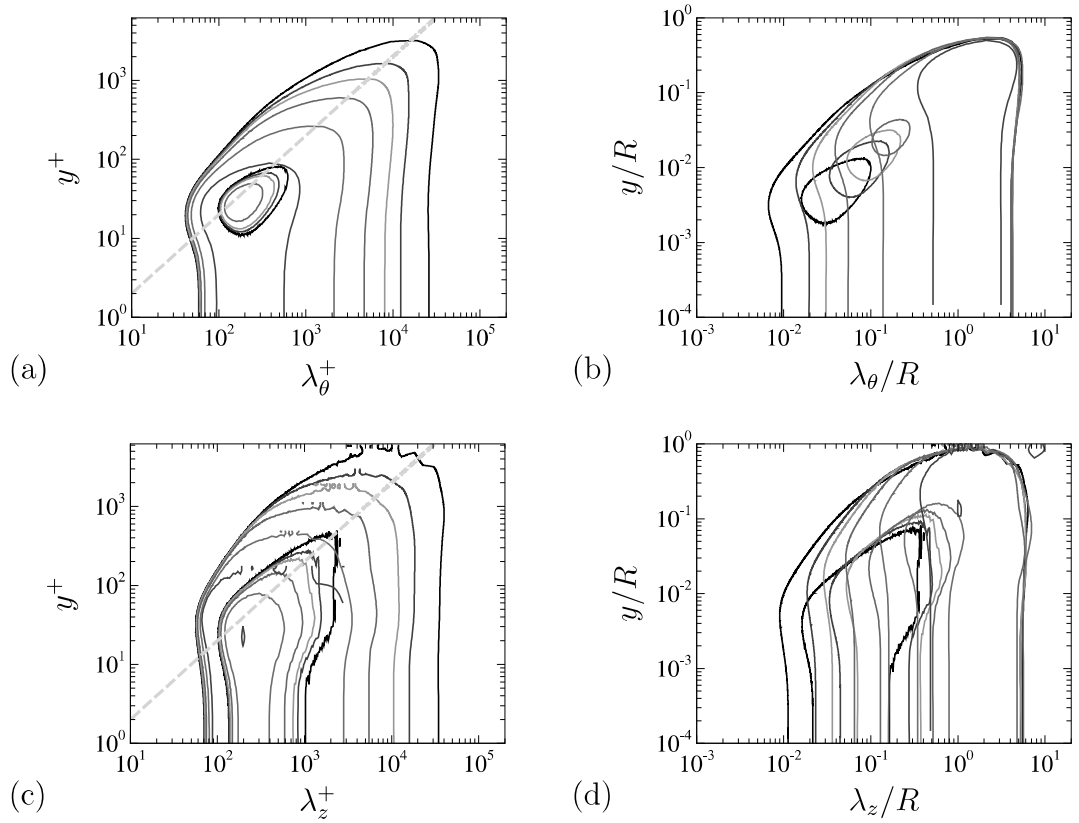

Figure 6: Pre-multiplied spectral densities of pressure fluctuations, (a,b) $k_\theta E_\theta^+$ and (c,d) $k_z E_z^+$, under (a,c) viscous and (b,d) outer coordinates. Line colors as in table 1. Contour levels: (a,b) 0.3 and 1.2, (c,d) 0.2 and 1.0. Grey dashed lines in panels (a) $\lambda_\theta = 5y$, (c) $\lambda_z = 5y$.

streaks [see, e.g. 21]. At higher Reynolds number (panels(c-f)), the multi-scale nature of pressure fluctuations becomes obvious. In particular, the small-scale eddies (see the zoomed inset), have similar characteristic length scales in the axial and azimuthal directions, thus showing no preferential alignment. On the other hand, the largest eddies come in the form of spanwise-aligned streaks, hence far from isotropy. Pressure fluctuations in the pipe cross section come in the form of blobs, whose size does not change substantially with the Reynolds number, and which are mainly distributed within the buffer layer. The figure further suggests (note that the same color scale is used for all cases) that extreme positive and negative pressure fluctuation events become stronger at higher Reynolds number.

More quantitative insight is provided by the spectra of pressure fluctuations, which are shown in figure 6, in pre-multiplied form. The spectral distributions

in the near-wall region ($y^+ \lesssim 100$) are close to being universal in wall units at small scales, although the peak intensity is slightly increasing with Re_τ. Most energetic contributions come from eddies residing at $y^+ \approx 30$, and with typical length scale $\lambda_\theta^+ \approx \lambda_z^+ \approx 200$ (see panels a,c), where λ_θ and λ_z are wavelengths along the azimuthal and axial directions, respectively. Similar insensitivity from Reynolds number variation in the wall-normal location and characteristic length scales of the spectral peaks was also found in channel flows [16]. Consistent with the attached nature of pressure as a flow variable, we find that the azimuthal and axial spectra both exhibit a prominent ridge which reaches out towards the top-right corner of the maps, suggesting linear growth of the length scales with the wall distance. When expressed in outer units (panels b, d) the spectra show very good universality at the largest scales. Unlike the axial velocity, the spectra of pressure fluctuations do not feature prominent outer-layer energetic peaks. However, the nearly vertical contour lines indicate that energetic pressure fluctuations at large scales ($\lambda_\theta \approx R$ and $\lambda_z \approx R$) penetrate through the logarithmic and the buffer layer at almost constant intensity down to the wall. In fact, unlike velocity fluctuations, pressure fluctuations are not constrained from the no-slip and/or no-penetration conditions which would cause them to decay in the wall proximity.

Reynolds number trends are better illustrated in figure 7, where we show peak values with respective wall distance and associated wavelength. The peak spectral amplitudes are found to increase very slowly, tending to reach an asymptotic value at high Reynolds number. Hence, the previously observed logarithmic increase of the peak pressure variances with Re_τ, is due to broadening of the range of eddy scales contributing to it, as figure 6 well illustrates, and as pointed out by Jimenez and Hoyas [9]. The position and the typical length scales of the near-wall spectral peak are also not changing much with Re_τ, and they are similar for the azimuthal and the axial spectra.

The wall pressure spectra are shown in detail in figure 8. When plotted against viscous scales, the spectral intensities are Reynolds number independent for $\lambda_\theta^+ \lesssim 100$, $\lambda_z^+ \lesssim 100$ for cases with $Re_\tau \gtrsim 1000$, consistent with the discussions on figure 7. The peak values are slowly increasing with the Reynolds number, and are attained at $\lambda_\theta^+ \approx 220$, $\lambda_z^+ \approx 250$. Notably, the azimuthal spectra seem to be more affected from Reynolds number variation than the axial ones. When plotted against outer coordinates, the spectra at the large scales become nearly Reynolds

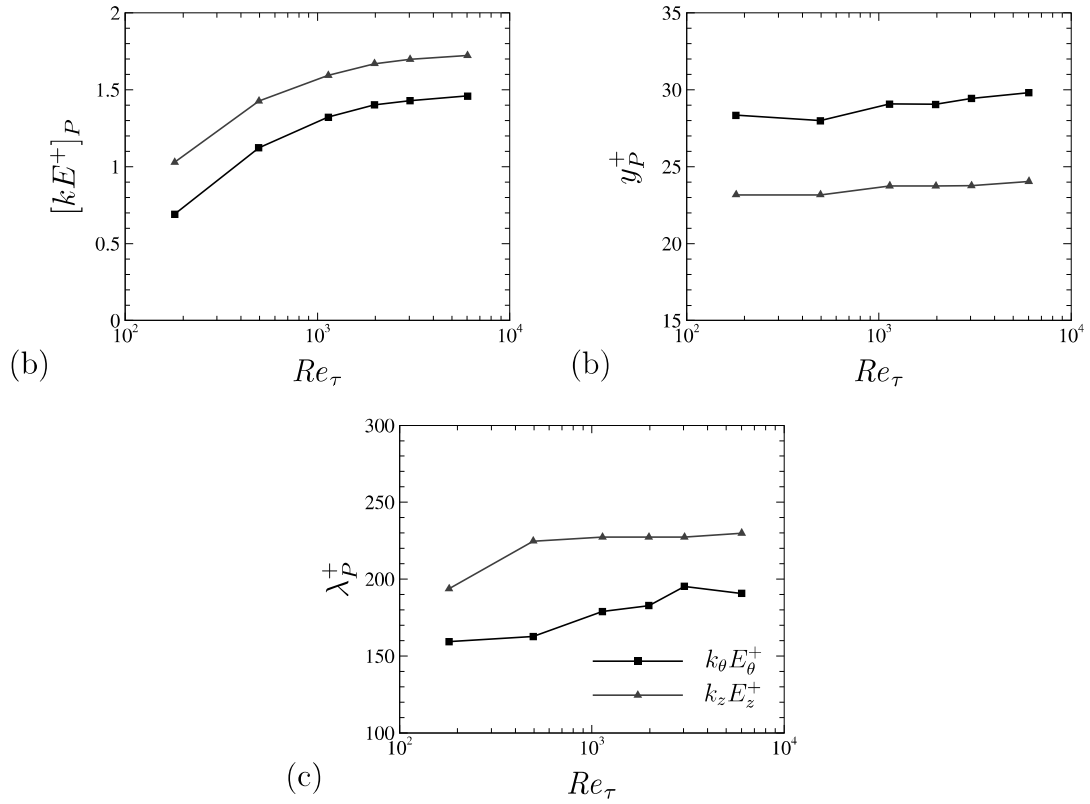

Figure 7: Reynolds number dependence of spectral peak values $[kE^+]_P$ (a), with corresponding wall-normal location y_P^+ (b), and associated wavelength λ_P^+ (c).

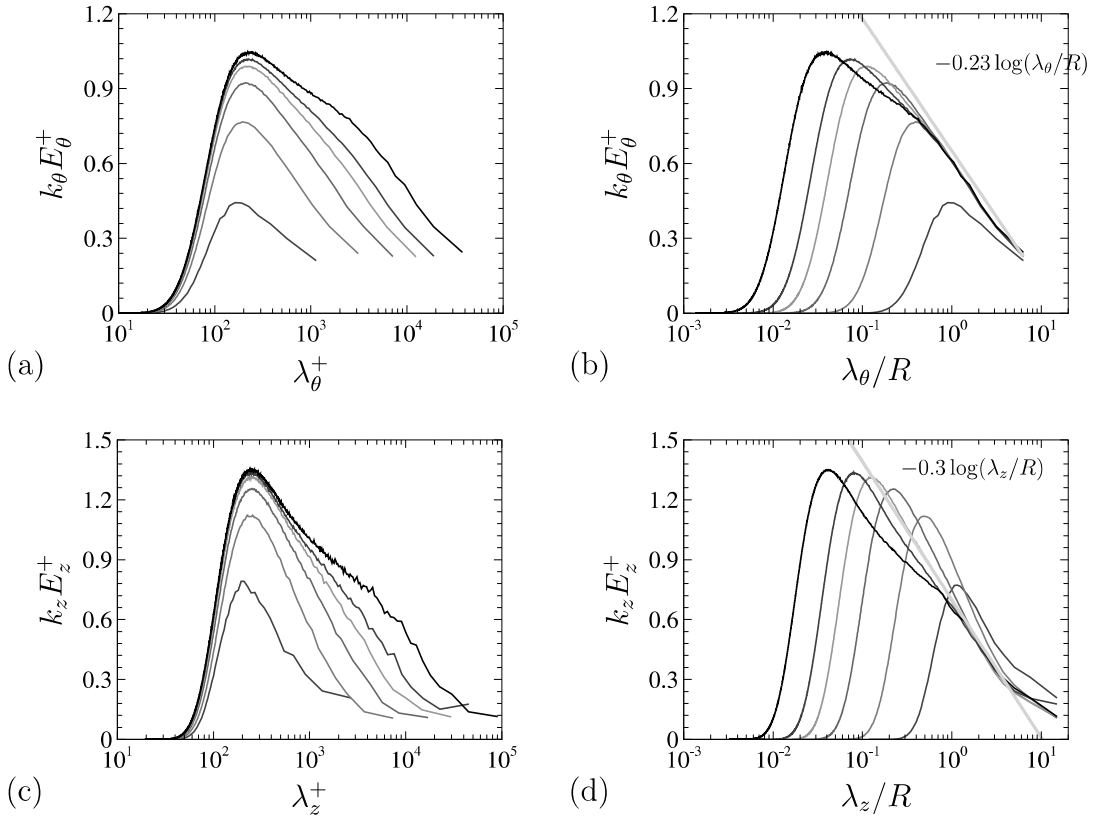

Figure 8: Pre-multiplied (a-b) azimuthal and (c-d) axial spectral densities of wall pressure, plotted under (a,c) viscous scales, (b,d) outer scales. Line colors as in table 1.

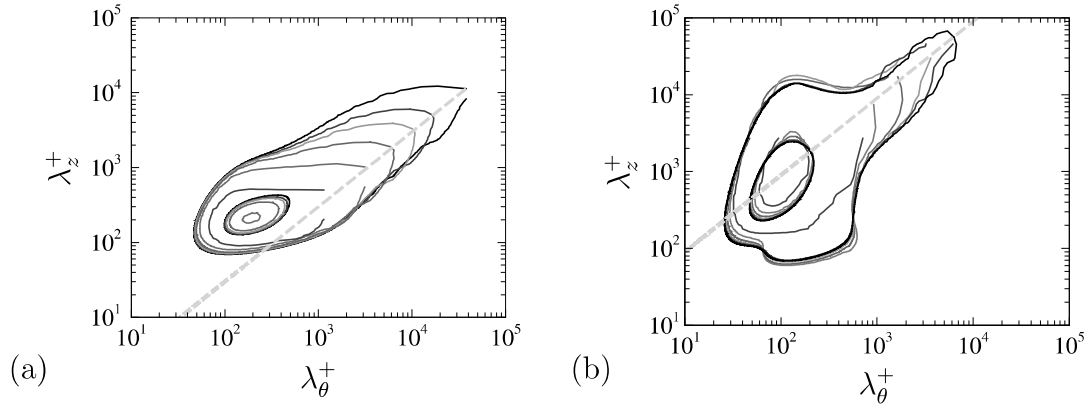

Figure 9: Two-dimensional pre-multiplied spectral densities ($k_\theta k_z E^+_{\theta z}$) of p' (a) and of $\partial u'_z/\partial y$ (b) at the wall. Contour lines: (a) 0.1 and 0.4, (b) 0.0004 and 0.002. Dashed lines in (a): $\lambda_z^+ = 0.3\lambda_\theta^+$, (b) $\lambda_z^+ = 10\lambda_\theta^+$. Line colors as in table 1.

number independent, as suggested by collapse of the contour lines in the large-λ range when outer scaling is used, see figure 6. In particular, universal distributions are achieved for $\lambda_\theta/R > 0.5$ in the azimuthal spectra, and for $\lambda_z/R > 2.0$ in the axial spectra, for $Re_\tau > 500$. The collapsed portion of the azimuthal and axial spectra seem to follow a logarithmic decay, with slope -0.23 and -0.3, respectively, although we could not find any convincing theoretical explanation.

The two-dimensional spectral densities of wall pressure are displayed in figure 9(a). The two-dimensional maps are consistent with the one-dimensional spectra discussed above, in that the spectra tend to be Reynolds number independent at small scales and at large scales when plotted against viscous and outer coordinates, respectively. Most energy resides at small scales, with peak at $\lambda_\theta^+ \approx 190$, $\lambda_z^+ \approx 210$, showing that these eddies are very nearly isotropic in the wall-parallel directions, as also found in channels [38, 9, 4]. As for the large-scale portion of the spectra, the characteristic length scales in the azimuthal direction are found to be roughly three times larger than in the axial direction, hence they are characterized by strong anisotropy. These results quantitatively corroborate our previous observations about the instantaneous pressure fields that the small-scale fluctuations tend to be isotropic, whereas the large-scale fluctuations are significantly elongated in the azimuthal direction. As a comparison, in turbulent channel flow the characteristic length scales of pressure fluctuations in the streamwise and spanwise directions in the outer region have been reported to be close to the half-channel

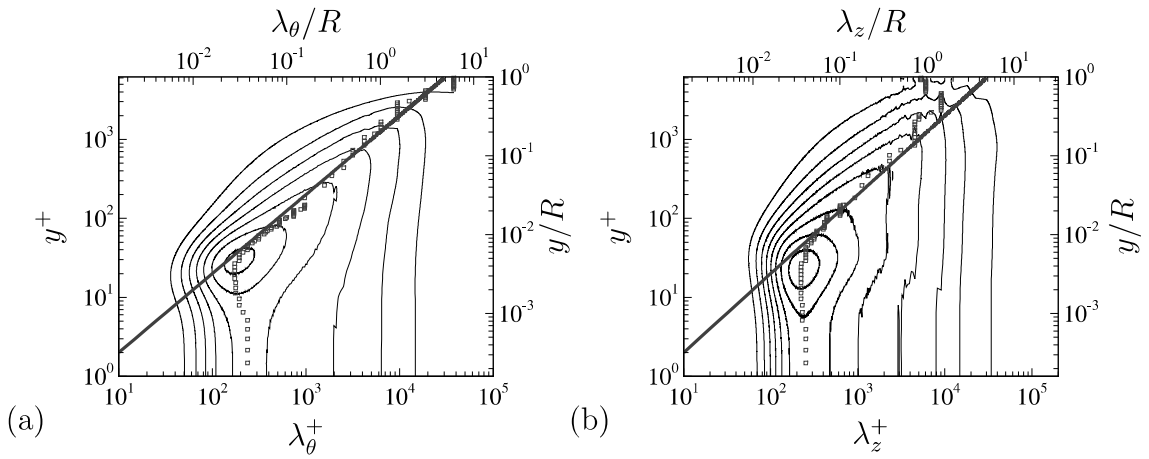

Figure 10: Pre-multiplied azimuthal (a) and axial (b) spectra of p', for DNS-F. The symbols denote the position of the spectral peak at any given y. The red lines denote the trends: (a) $\lambda_\theta^+ = 5y^+$, (b) $\lambda_z^+ = 5y^+$.

height [16]. A recent study [39] based on resolvent analysis applied to turbulent channel flow at low Reynolds numbers, likewise predicted that the energetic large-scale pressure fluctuations are spanwise oriented. In particular, resolvent analysis predicts the presence of spanwise-coherent modes displaying alternating spanwise vortices, with pressure peaking at the vortex centers.

This is to be contrasted with the structure of the axial velocity field in the wall proximity, which are shown in figure 9(b). Also in this case the spectral maps are bi-modal, however both small eddies and large eddies tend to be elongated along the axial direction, with aspect ratio of about ten, corresponding to near-wall streaks, and to the imprinting of outer-layer superstructures.

The spectral distributions in the logarithmic region are inspected next. For that purpose, we only show results for DNS-F, in which a logarithmic region is most evident. As a first step, we have detected the peak values of the spectra at each wall-normal locations, and marked them with symbols in figure 10. Between the peak locations in the near-wall region at $y^+ \approx 30$ and $y^+ \approx 1000$ (corresponding to $y/R \approx 0.17$), the characteristic length scales in both the azimuthal and axial directions increase linearly with the wall-normal coordinate, showing close similarity. The slope of this linear trend is approximately 5.0, which is higher than the value 3.0 reported for turbulent channels [9, 16].

Based on the observation that the pressure fluctuations are most energetic at

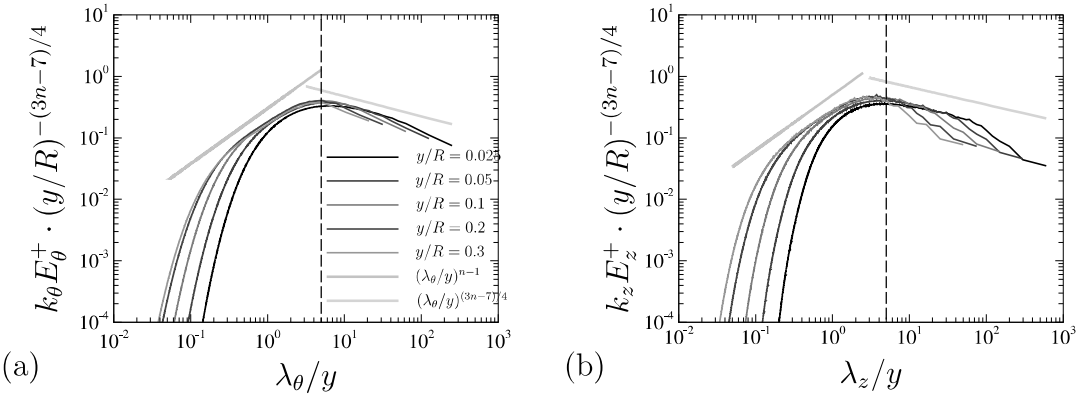

Figure 11: Compensated azimuthal spectra (a) and axial spectra (b) for DNS-F at several wall distances ($y/R = 0.025$, 0.05, 0.1, 0.2 and 0.3), as a function of wall distance-scaled wavelength ($n = 1.9$). The vertical dashed lines correspond to $\lambda/y = \kappa$ (here $\kappa = 5.0$).

small scales, Xu et al. [20] inferred scaling laws for the streamwise pressure spectra, relying on Kolmolgorov theory and on the attached-eddy hypothesis, which can be formulated as

$$y^{-(3n-7)/4}[k_x E_x] \sim (\lambda_x/y)^{n-1}, \tag{7}$$

for $\lambda_x < \kappa y$, and

$$y^{-(3n-7)/4}[k_x E_x] \sim (\lambda_x/y)^{(3n-7)/4}, \tag{8}$$

for $\lambda_x > \kappa y$, where κ denotes the slope of the linear relation in figure 10. The parameter n was found to be in general dependent on the local Taylor micro-scale Reynolds number. Herein we attempt to validate their theory in pipe flow. In figure 11, we thus display compensated, pre-multiplied spectra of pressure, namely $(y/R)^{-(3n-7)/4} k_\theta E_\theta^+$, $(y/R)^{-(3n-7)/4} k_z E_z^+$ for the DNS-F flow case, at $y/R = 0.025$, 0.05, 0.1, 0.2 and 0.3. Best fitting of the dataset yields $n = 1.9$, consistent with the results reported by Xu et al. [20], Tsuji et al. [3] in turbulent channels. At small length scales, the power-law (7) is satisfied in an increasingly wide band of wavelengths at increasing wall distance, up to about one decade. The scaling (8) is found to hold for $\lambda_\theta/y > 5$ and $\lambda_z/y > 5$, in a wider range as the wall is approached, which indicates that band of wavenumbers is a constant fraction of R. Although the scaling laws in equations (7) and (8) were derived for the streamwise spectra in channels, we find that the conclusions apply to pipes as well, also in the azimuthal direction.

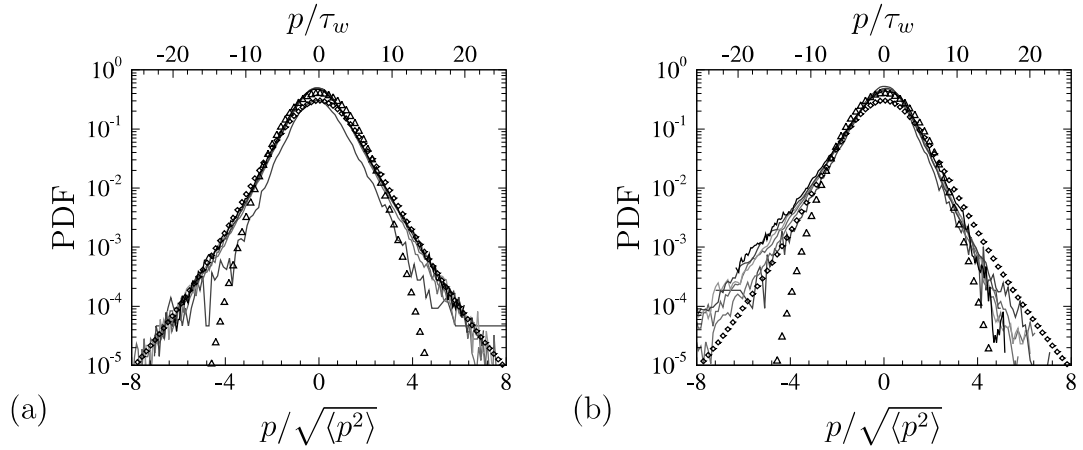

Figure 12: Normalized probability density distributions of pressure fluctuations at (a) wall; and (b) $y = 0.2R$. Triangles: Gaussian distribution, diamonds: T-distribution. The top axis reports a scale p/τ_w for the DNS-F flow case.

Figure 12 displays the probability density distributions of pressure fluctuations at the wall and at $y = 0.2R$. Consistent with previous observations [8], we find that positive and negative pressure fluctuations are equally likely to occur at the wall, hence the skewness is locally zero. As the Reynolds number increases, the frequency of intense pressure fluctuations increases, and algebraic tails. The resulting probability density function is quite far from Gaussian (triangles), and we empirically find that it can conveniently be approximated as a T-distribution,

$$PDF(x) = \frac{(n-2)\Gamma\left(\frac{n+1}{2}\right)}{n\sqrt{n\pi}\Gamma\left(\frac{n}{2}\right)}\left(1+\frac{x^2}{n}\right)^{-(n+1)/2}, \tag{9}$$

where Γ is the Gamma function, by setting $n = 9$. According to its definition, the T-distribution is similar to the normal distribution but has fatter tails, with normal distribution recovered in the limit $n \to \infty$. Hence, finite value of the parameter n has to do with the strong observed intermittency of the pressure fluctuations.

At $y = 0.2R$, the most intense pressure fluctuations become negative, and the structure of the PDF are similar to those reported for isotropic turbulence [40]. In particular, whereas negative fluctuations still exhibit an exponential tail, positive fluctuations are more nearly Gaussian. This has to do with the fact that the most intermittent structures in isotropic turbulence are tube-like vortices, with low-pressure at their interior [41].

5. Outer-layer similarity and wall-attached eddies

The spectral maps discussed in the previous section have shown that the large-scale, pressure-bearing eddies are nearly Reynolds number independent, and that pressure fluctuations in the logarithmic region show some typical features of self-similarity resulting from wall-attached eddies. To further elaborate on this issue, herein we exploit proper orthogonal decomposition (POD) to extract the structures with strongest spatial coherence, as previously done by many authors to analyse transitional and turbulent flows [e.g. 42, 43, 44]. For that purpose we have collected five hundred cross-stream planes for each case, which proved to be sufficient to achieve statistical convergence of the ensemble. Considering homogeneity and periodicity in the azimuthal direction, we then proceed as suggested by Hellström et al. [45], by expanding the flow properties in Fourier series, leaving only spatial coherence in the radial direction to be determined. The two-point correlation tensor of the azimuthal spectral coefficients is expressed as

$$S(k_\theta, r, r') = \lim_{T\to\infty} \int_0^T r^{1/2} \hat{p}(k_\theta, r, t) \hat{p}^*(k_\theta, r', t) r'^{1/2} \mathrm{d}t, \tag{10}$$

where the hat symbols is used to denote the Fourier coefficients, and the asterisk to denote the complex conjugate. The POD equation can then be cast as

$$\int_{r'} S(k_\theta, r, r') \phi^{(n)}(k_\theta, r') \mathrm{d}r' = \sigma^{(n)}(k_\theta) \phi^{(n)}(k_\theta, r) \sqrt{r}, \tag{11}$$

with $\sigma^{(n)}(k_\theta)$ and $\phi^{(n)}(k_\theta, r)$ denoting energy and associated radial profiles of the $n-$th POD mode corresponding to the azimuthal wavenumber k_θ. In a discretized setting, we collect all data samples into a matrix

$$\boldsymbol{X} = [\boldsymbol{x}_1, \boldsymbol{x}_2, \cdots, \boldsymbol{x}_N], \tag{12}$$

whose column vectors $\boldsymbol{x}_i$ $(i = 1, 2, \cdots, N)$ are

$$\boldsymbol{x}_i = [x_{1i}, x_{2i}, \cdots, x_{N_r i}]'. \tag{13}$$

We further set $x_{ij} = \hat{p}(k_\theta, r_j, t_i)\Delta r_j$ to incorporate the grid intervals so that the correlation and the POD energy is consistent with the definition given in equations (10), (11). The POD for the discretized system is then obtained from singular value decomposition of matrix $\boldsymbol{X}$,

$$\boldsymbol{X} = \boldsymbol{U}\boldsymbol{\Sigma}'\boldsymbol{V}^H, \quad \boldsymbol{U} \in \boldsymbol{C}^{N_r \times N}, \quad \boldsymbol{\Sigma}' \in \boldsymbol{C}^{N\times N}, \quad \boldsymbol{V} \in \boldsymbol{C}^{N\times N}, \tag{14}$$

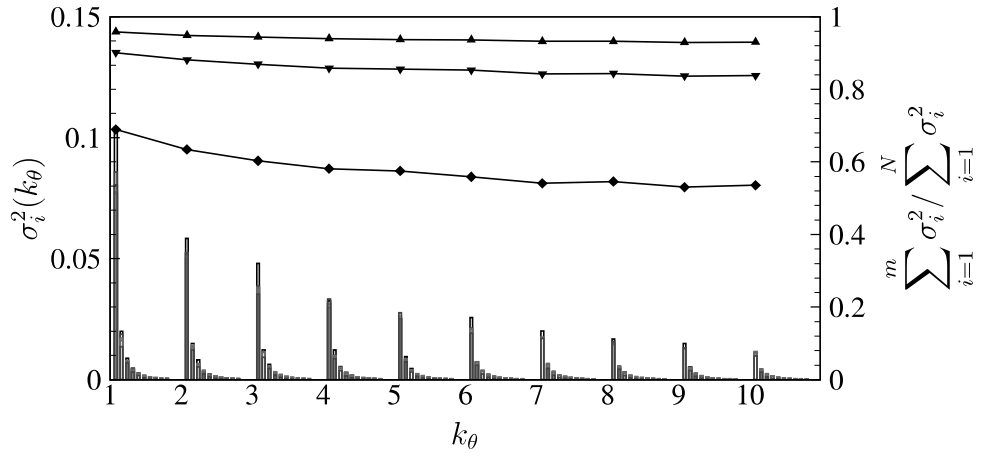

Figure 13: POD modal energy for the first ten azimuthal wavenumbers k_θ (bar charts, left ordinate) and cumulated energy of the first 1 , 3 and 5 modes (lines, right ordinate), the DNS-F flow case.

where $\boldsymbol{U}$ and $\boldsymbol{V}$ are unitary matrices, and $\boldsymbol{\Sigma}'$ is the diagonal matrix whose elements are the singular values,

$$\boldsymbol{\Sigma}' = \mathrm{diag}\{\sigma'_1, \sigma'_2, \cdots, \sigma'_N\}, \tag{15}$$

which are related to the POD modal energy as $\sigma_i^2 = \sigma_i'^2/N$. The corresponding POD modes are the columns of matrix $\boldsymbol{U}$.

Figure 13 displays the energy of the first ten POD modes associated with the first ten azimuthal wavenumbers. The first azimuthal mode is found to be the most energetic, and for each azimuthal mode, the first POD mode is found to be much more energetic than the others, containing about 60% of the energy. The first three and the first five modes take up more than 80% and 90% of the energy, respectively.

To examine the Reynolds number dependence of the large-scale motions, the modal profiles for the first four azimuthal wavenumbers are shown in figure 14, normalized by their respective maximum values. For each azimuthal wavenumber the first POD mode has a main peak at $y \approx 0.2 \sim 0.3R$, which is consistent with the spectral distribution shown in figure 6(b). Because there is no restriction from the no-slip and no-penetration conditions as for velocity, the amplitude of these modes is not zero at the wall, but rather it is approximately 80% of the maximum

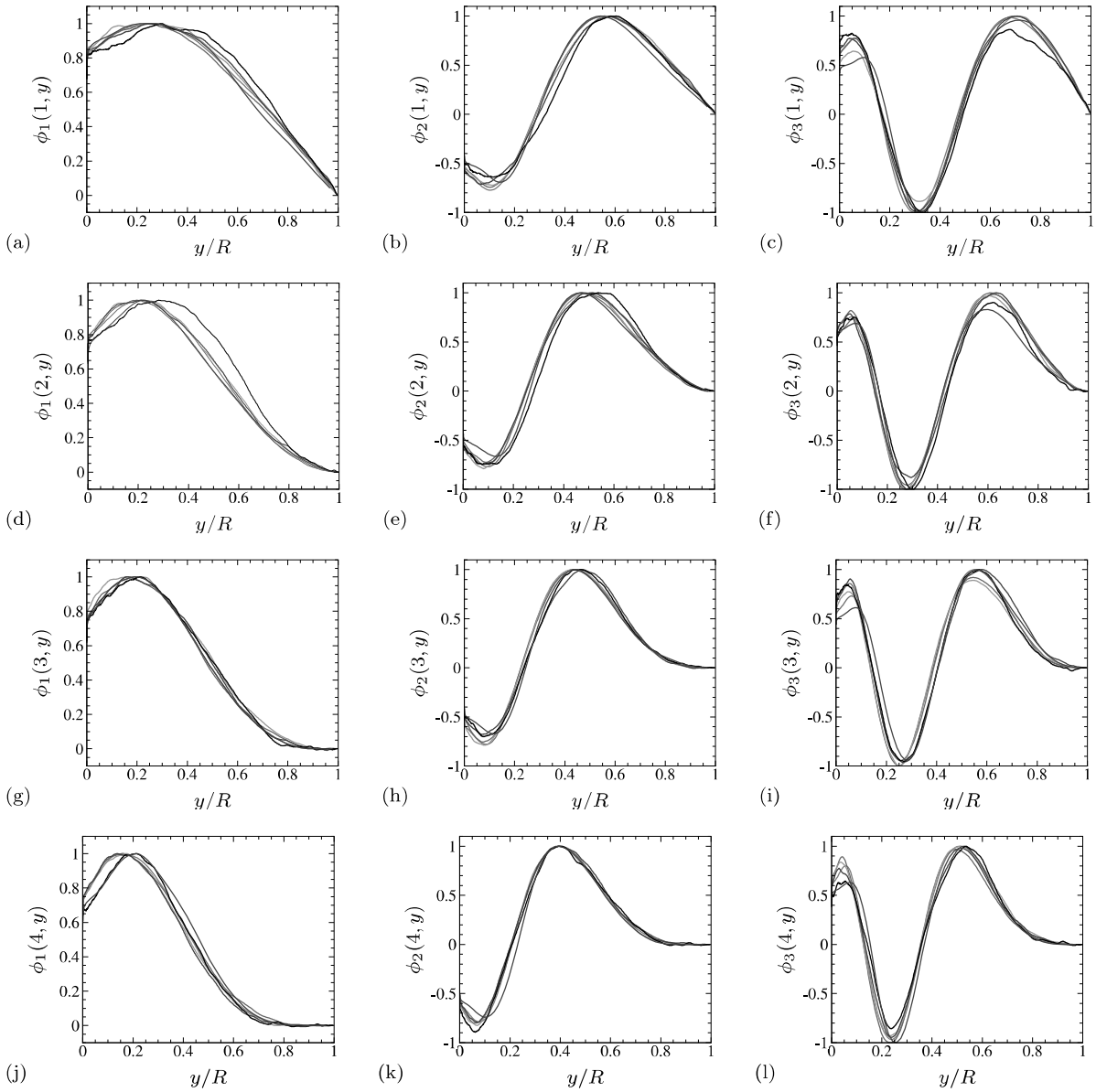

Figure 14: Radial profiles of POD modes, each normalized by its maximum value, for $k_\theta = 1$ (a-c), $k_\theta = 2$ (d-f), $k_\theta = 3$ (g-i), $k_\theta = 4$ (j-l): mode 1 (a,d,g,j), mode 2 (b,e,h,k), mode 3 (c,f,i,l). Line colors as in table 1.

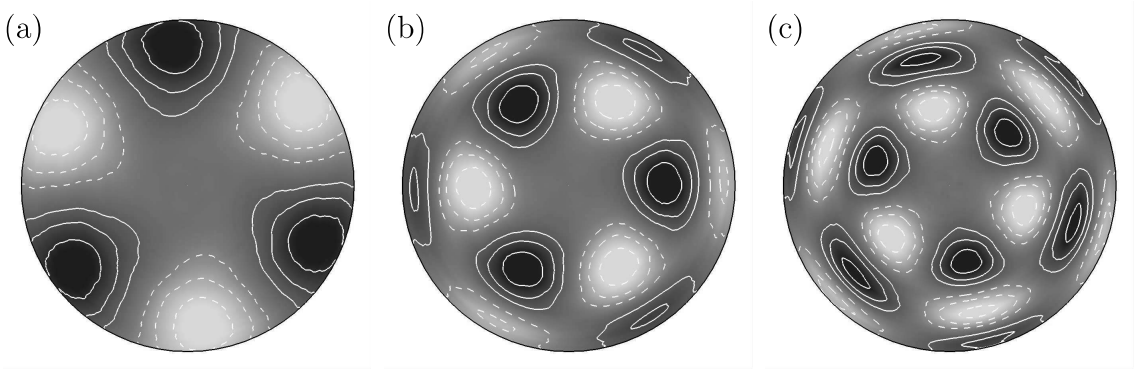

Figure 15: Cross-stream shape of POD modes corresponding to $k_\theta = 3$, for DNS-F flow case: (a) mode 1, (b) mode 2, (c) mode 3.

value. The second and the third POD modes are comparatively less energetic, and peaks and troughs gradually move closer to the wall as the azimuthal wavenumber increases. For those modes, the wall values are about 50% of the maximum value. In general, the modal profiles are well collapsed for different Reynolds number cases, supporting our previous observations that outer energetic motions are very much Reynolds number independent. A visual impression for a particular family of azimuthal modes (corresponding to $k_\theta = 3$) is provided in figure 15, showing a full reconstruction in the pipe cross-stream plane.

We further seek evidence for self-similarity (or not) of the pressure-bearing eddies. In figure 16, we thus plot the wall distance of the main peak, for the first POD modes corresponding to each azimuthal wavenumber, say y_p. Only cases at $Re_\tau > 1000$ are shown, as lower Reynolds numbers do not feature any significant logarithmic region. The figure shows that within the range of wavenumbers $k_\theta R \gtrsim 10$, the wall-normal location scales approximately as $y_p/R = 2\pi C(k_\theta R)^{-1}$, with $C \approx 0.2$. This result is very close to what reported by Hellström et al. [45] for velocity fluctuations resulting from pipe flow experiments. This finding supports the notion that the sizes of the most energetic pressure-bearing eddies are proportional to their center locations from the wall, thus corroborating observations made regarding the one-dimensional spectral distributions (see figure 10).

The normalized profiles of the first three POD modes at $k_\theta = 10$, 20 and 30 are shown in figure 17, for cases with $Re_\tau > 1000$, with the wall distance scaled by the azimuthal wavenumber. The first POD modes have relative amplitude 0.7

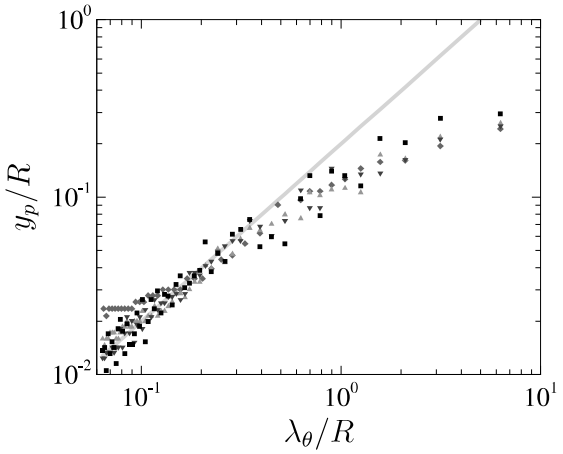

Figure 16: Peak locations of first POD mode for azimuthal wavenumbers $k_\theta \in [1, 100]$, The grey line marks the trend $y_p = C\lambda_\theta$ ($\lambda_\theta = 2\pi/k_\theta$) with $C = 0.2$. Colors denote the various flow cases, as given in table 1.

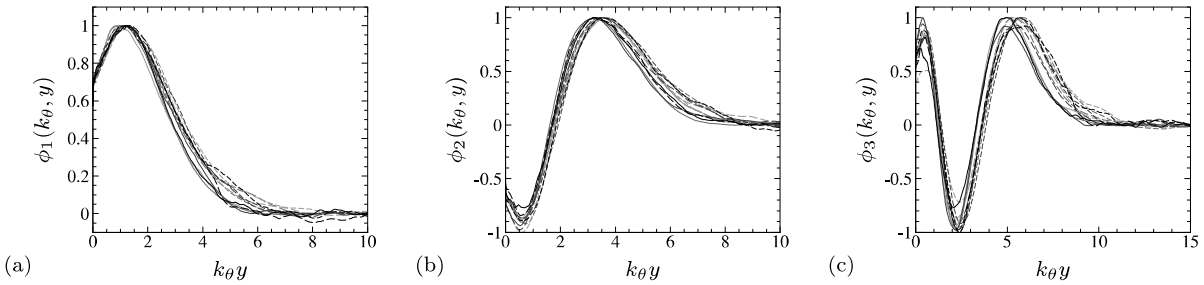

Figure 17: Shapes of POD modes for $k_\theta = 10$ (solid), $k_\theta = 20$ (dashed), $k_\theta = 30$ (dot-dashed), scaled by the wall distance: (a) mode 1, (b) mode 2, (c) mode 3. Line colors as in table 1.

at the wall, attain a maximum at $k_\theta y \approx 1$, and drop to zero at $k_\theta y \approx 6$. The second modes have wall value of about -0.7, attain a minimum at $k_\theta y \approx 0.5$, and a peak value at $k_\theta y \approx 3.0$. The profiles then drop to zero at $k_\theta y \approx 8.0$. The third modes behave similarly, except for an additional zero crossing. These POD modes exhibit clear self-similarity as their profiles are well collapsed under the normalized coordinate $k_\theta y$, but they are also very nearly universal with respect to Reynolds number variation.

6. Concluding comments

Availability of a DNS database is a convenient way to gain information about the structure of pressure fluctuations in internal flows, as done here for pipe flow. Although similarities with previous studies dealing with channel flow are clear, some differences are worth being mentioned, and some flow features herein observed were not previously noted, also because of Reynolds number limitations. Regarding the basic statistics, we note that the mean pressure in pipe flow has a different structure than in channel flow, mainly owing to the presence of an extra term in the mean balance equation, which is associated with combined centrifugal and swirling effects. As a result, the peak pressure difference with respect to the wall is larger in pipes, and it occurs much farther from the wall, at $y/R \approx 0.2$. The pressure variance shows an absolute peak within the buffer layer associated with extreme turbulence activity, and farther from the wall shows a very distinct logarithmic decline, at slightly lower rate than in channels. Logarithmic growth of the wall pressure with the friction Reynolds number is also observed, at a slightly smaller rate than in channels. Put together, the evidence supports the notion that the pressure-bearing eddies should constitute a hierarchy of wall-attached eddies, as speculated in theoretical models for the behavior of the axial velocity fluctuations. Here the evidence is even clearer, as pressure in the wall vicinity is not attenuated from the no-slip condition as the velocity. The computed pressure spectral maps in fact support this notion, and show a typical imprint consisting of a main buffer-layer peak at $y^+ \approx 30$, and typical wavelength $\lambda^+ \approx 200$ in both wall-parallel directions, and a spectral ridge featuring eddies with wavelengths linearly proportional to the wall distance, which are also found to be quasi-isotropic. Self-similarity of the spectra in the range of wall distances from $y^+ \approx 50$ to $y/R \approx 0.2$ is shown, and their shape is found to conform well with a recent conceptual model.

The wall pressure fluctuations, which have obviously the highest practical interest, include contributions from eddies of all size, which manifest themselves in instantaneous flow realizations as nearly circular blobs (near-wall and attached eddies), and as azimuthally elongated streaks, limited to the largest $O(R)$-sized eddies. Understanding how these wide azimuthal wall pressure signatures are related to a particular class of coherent structure could be an interesting subject for future research. The wall pressure fluctuations are found to have nearly zero skewness and heavy exponential tails, which indicate the importance of relatively rare events. This peculiar structure should be contrasted with what found away from the wall, where the structure of pressure fluctuations is similar to isotropic turbulence, with strong negative tails, and near-Gaussian positive tails. Proper orthogonal decomposition has been used to quantitatively extract the shape of the energetically relevant modes, upon Fourier expansion in the azimuthal direction. We have found that higher azimuthal modes are associated with progressively smaller distance from the wall, and they tend to be very much universal, which provides a tangible manifestation of the hierarchy of wall-attached eddies.

Acknowledgements

This project has been partially funded from the Programma Operativo Nazionale (PON) of the Italian Ministry of University and Research, under grant 'Generazione E'. The results reported in this paper have been achieved using the PRACE Research Infrastructure resource MARCONI based at CINECA, Casalecchio di Reno, Italy, under project PRACE n. 2019204979.

References

[1] W. Blake, Mechanics of flow-induced sound and vibration, Volume 2: Complex flow-structure interactions, Academic press, 2017.

[2] T. Farabee, M. Casarella, Spectral features of wall pressure fluctuations beneath turbulent boundary layers, Phys.Fluids 3 (1991) 2410–2420.

[3] Y. Tsuji, J. Fransson, P. Alfredsson, A. Johansson, Pressure statistics and their scaling in high-Reynolds-number turbulent boundary layers, J. Fluid .Mech. 585 (2007) 1–40.

[4] J. Klewicki, P. Priyadarshana, M. Metzger, Statistical structure of the fluctuating wall pressure and its in-plane gradients at high Reynolds number, J. Fluid Mech. 609 (2008) 195–220.

[5] G. Lauchle, M. Daniels, Wall-pressure fluctuations in turbulent pipe flow, Phys. Fluids 30 (1987) 3019–3024.

[6] Y. Tsuji, S. Imayama, P. Schlatter, P. Alfredsson, A. Johansson, I. Marusic, N. Hutchins, J. Monty, Pressure fluctuation in high-Reynolds-number turbulent boundary layer: results from experiments and DNS, J. Turbul. 13 (2012) N50.

[7] W. Willmarth, Pressure fluctuations beneath turbulent boundary layers, Annu. Rev. Fluid Mech. 7 (1975) 13–36.

[8] Z. Hu, C. Morfey, N. Sandham, Wall pressure and shear stress spectra from direct simulations of channel flow, AIAA J. 44 (2006) 1541–1549.

[9] J. Jimenez, S. Hoyas, Turbulent fluctuations above the buffer layer of wall-bounded flows, J. Fluid Mech. 611 (2008) 215–236.

[10] J. Sillero, J. Jiménez, R. Moser, One-point statistics for turbulent wall-bounded flows at Reynolds numbers up to $\delta^+ \approx 2000$, Phys. Fluids 25 (2013) 105102.

[11] A. Townsend, The Structure of Turbulent Shear Flow, 2nd edn. Cambridge University Press., 1976.

[12] Y. Hwang, Statistical structure of self-sustaining attached eddies in turbulent channel flow, J. Fluid Mech. 767 (2015) 254–289.

[13] I. Marusic, J. Monty, Attached eddy model of wall turbulence, Annu. Rev. Fluid Mech. 51 (2019) 49–74.

[14] P. Bradshaw, 'inactive'motion and pressure fluctuations in turbulent boundary layers, J. Fluid Mech. 30 (1967) 241–258.

[15] R. Panton, M. Lee, R. Moser, Correlation of pressure fluctuations in turbulent wall layers, Phys. Rev. Fluids 2 (2017) 094604.

[16] A. Mehrez, J. Philip, Y. Yamamoto, Y. Tsuji, Pressure and spanwise velocity fluctuations in turbulent channel flows: Logarithmic behavior of moments and coherent structures, Phys. Rev. Fluids 4 (2019) 044601.

[17] S. Ghaemi, F. Scarano, Turbulent structure of high-amplitude pressure peaks within the turbulent boundary layer, J. Fluid Mech. 735 (2013) 381–426.

[18] M. Luhar, A. Sharma, B. McKeon, On the structure and origin of pressure fluctuations in wall turbulence: predictions based on the resolvent analysis, J. Fluid Mech. 751 (2014) 38–70.

[19] Y. Tsuji, I. Marusic, A. Johansson, Amplitude modulation of pressure in turbulent boundary layer, Int. J. Heat Fluid Flow 61 (2016) 2–11.

[20] H. Xu, A. Towne, X. Yang, I. Marusic, Pressure power spectrum in high-Reynolds number wall-bounded flows, Int. J. Heat Fluid Flow 84 (2020) 108620.

[21] S. Pirozzoli, J. Romero, M. Fatica, R. Verzicco, P. Orlandi, One-point statistics for turbulent pipe flow up to $Re_\tau = 6000$, J. Fluid Mech. 926 (2021).

[22] F. Harlow, J. Welch, Numerical calculation of time-dependent viscous incompressible flow of fluid with free surface, Phys. Fluids 8 (1965) 2182–2189.

[23] J. Kim, P. Moin, Application of a fractional-step method to incompressible Navier-Stokes equations, J. Comput. Phys. 59 (1985) 308–323.

[24] R. Verzicco, P. Orlandi, A finite-difference scheme for three-dimensional incompressible flows in cylindrical coordinates, J. Comput. Phys. 123 (1996) 402–414.

[25] K. Akselvoll, P. Moin, An efficient method for temporal integration of the Navier–Stokes equations in confined axisymmetric geometries, J. Comput. Phys. 125 (1996) 454–463.

[26] X. Wu, P. Moin, A direct numerical simulation study on the mean velocity characteristics in turbulent pipe flow, J. Fluid Mech. 608 (2008) 81–112.

[27] G. Ruetsch, M. Fatica, CUDA Fortran for scientists and engineers, Elsevier, 2014.

[28] S. Pirozzoli, P. Orlandi, Natural grid stretching for DNS of wall-bounded flows, J. Comput. Phys. 439 (2021) 110408.

[29] J. Jiménez, Coherent structures in wall-bounded turbulence, J. Fluid Mech. 842 (2018).

[30] S. Pirozzoli, M. Bernardini, P. Orlandi, Passive scalars in turbulent channel flow at high Reynolds number, J. Fluid Mech. 788 (2016) 614–639.

[31] S. Hoyas, J. Jiménez, Scaling of velocity fluctuations in turbulent channels up to $Re_\tau = 2003$, Phys. Fluids 18 (2006) 011702.

[32] M. Lee, R. Moser, Direct numerical simulation of turbulent channel flow up to $Re_\tau \approx 5200$, J. Fluid Mech. 774 (2015) 395–415.

[33] J. Ahn, J. Lee, J. Lee, J.-H. Kang, H. Sung, Direct numerical simulation of a 30R long turbulent pipe flow at $\mathrm{Re}_\tau = 3000$, Phys. Fluids 27 (2015) 065110.

[34] S. Pirozzoli, J. Romero, M. Fatica, R. Verzicco, P. Orlandi, Dns of passive scalars in turbulent pipe flow, J. Fluid Mech. 940 (2022) A45.

[35] S. Russo, P. Luchini, A fast algorithm for the estimation of statistical error in DNS (or experimental) time averages, J. Comput. Phys. 347 (2017) 328–340.

[36] H. Schlichting, K. Gersten, Boundary layer theory, 8th edn. Springer-Verlag, 2000.

[37] A. Smits, M. Hultmark, M. Lee, S. Pirozzoli, X. Wu, Reynolds stress scaling in the near-wall region of wall-bounded flows, J. Fluid Mech. 926 (2021) A31.

[38] J. Kim, On the structure of pressure fluctuations in simulated turbulent channel flow, J. Fluid Mech. 205 (1989) 421–451.

[39] F. Amaral, A. Cavalieri, Resolvent analysis of pressure fluctuations in turbulent channel flows, arXiv preprint arXiv:2108.10833 (2021).

[40] A. Pumir, A numerical study of pressure fluctuations in three-dimensional, incompressible, homogeneous, isotropic turbulence, Phys. Fluids 6 (1994) 2071–2083.

[41] J. Jiménez, A. A. Wray, On the characteristics of vortex filaments in isotropic turbulence, J. Fluid Mech. 373 (1998) 255–285.

[42] J. Lumley, The structure of inhomogeneous turbulent flows, Atmospheric turbulence and radio wave propagation (1967).

[43] P. Holmes, J. Lumley, G. Berkooz, C. Rowley, Turbulence, coherent structures, dynamical systems and symmetry, Cambridge university press, 2012.

[44] K. Taira, S. Brunton, S. Dawson, C. Rowley, T. Colonius, B. McKeon, O. Schmidt, S. Gordeyev, V. Theofilis, L. Ukeiley, Modal analysis of fluid flows: An overview, AIAA J. 55 (2017) 4013–4041.

[45] L. Hellström, I. Marusic, A. Smits, Self-similarity of the large-scale motions in turbulent pipe flow, J. Fluid Mech. 792 (2016).